nature
materials

Check for updates

Linking void and interphase evolution to electrochemistry in solid-state batteries using operando X-ray tomography

John A. Lewis[1], Francisco Javier Quintero Cortes[1], Yuhgene Liu[1], John C. Miers[2], Ankit Verma[3], Bairav S. Vishnugopi[3], Jared Tippens[2], Dhruv Prakash[1], Thomas S. Marchese[1], Sang Yun Han[2], Chanhee Lee[2,4], Pralav P. Shetty[2], Hyun-Wook Lee[4], Pavel Shevchenko[5], Francesco De Carlo[5], Christopher Saldana[2], Partha P. Mukherjee[3] and Matthew T. McDowell[1,2] ✉

Despite progress in solid-state battery engineering, our understanding of the chemo-mechanical phenomena that govern electrochemical behaviour and stability at solid–solid interfaces remains limited compared to at solid–liquid interfaces. Here, we use operando synchrotron X-ray computed microtomography to investigate the evolution of lithium/solid-state electrolyte interfaces during battery cycling, revealing how the complex interplay among void formation, interphase growth and volumetric changes determines cell behaviour. Void formation during lithium stripping is directly visualized in symmetric cells, and the loss of contact that drives current constriction at the interface between lithium and the solid-state electrolyte ($Li_{10}SnP_2S_{12}$) is quantified and found to be the primary cause of cell failure. The interphase is found to be redox-active upon charge, and global volume changes occur owing to partial molar volume mismatches at either electrode. These results provide insight into how chemo-mechanical phenomena can affect cell performance, thus facilitating the development of solid-state batteries.

Solid-state batteries (SSBs) have garnered interest due to their lack of hazardous liquid electrolytes, in addition to the potential of solid-state electrolytes (SSEs) being able to suppress lithium filament growth and thereby enable lithium metal anodes[1–4]. Despite the development of SSEs with high ionic conductivity[5], both the understanding of and control over solid electrode/SSE interfaces have emerged as major challenges in the development of SSBs[2,6–8]. In general, chemo-mechanical degradation is expected to be more severe in SSBs compared to liquid-electrolyte batteries because the SSE cannot flow like a liquid[2,6]. Understanding chemo-mechanical transformations at interfaces is therefore critical for engineering SSBs.

Most SSEs are unstable against lithium metal and decompose to form an interphase layer at the interface[9–11], with the transport properties and structure of the interphase playing a crucial role in determining the degradation pathways[12–15]. Additionally, SSEs that form passivating interphases (such as $Li_7La_3Zr_2O_{12}$ and the $Li_2S–P_2S_5$ system) are often vulnerable to lithium metal penetration and short circuiting[16–19], limiting cycling to current densities that are insufficient for commercial batteries[20]. Furthermore, maintaining mechanical contact at the Li/SSE interface during cycling is challenging. Morphological changes of electrode materials and interphases can result in contact loss or other mechanical damage[13,21–23]. Electrochemical studies have shown that Li/SSE interfaces are fundamentally limited by the formation of voids during lithium stripping[24,25], which reduces the contact area and creates larger local current densities that can drive lithium metal penetration.

Understanding these phenomena requires operando experiments for directly elucidating how solid-state interfaces evolve in real time. However, probing buried interfaces in SSBs necessitates techniques that can penetrate materials while providing local interfacial information. X-ray tomography is an excellent tool for studying buried interfaces as it yields three-dimensional reconstructions of materials with spatial resolution down to the sub-micron scale[26,27]. X-ray tomography has recently revealed how SSB cell performance is impacted by factors such as structure, porosity and the mechanical properties of materials[21,23,24,28–40]. Operando and multi-modal experiments have captured the evolution of cathodes and alloying anodes (such as tin and indium) during cycling[30–32], and such experiments have been able to image lithium metal within SSBs despite its weak X-ray attenuation[33,34]. However, only a relatively small number of X-ray imaging studies has investigated the interfaces between lithium metal electrodes and SSEs[23,25,34–38]. Furthermore, there have been no operando X-ray tomography experiments that have imaged void formation and Li/SSE interfacial contact during cycling to enable quantitative linkage to electrochemical behaviour, which is critical for improving our understanding of SSB operation.

In this Article, we used operando synchrotron X-ray computed microtomography to observe dynamic phenomena in $Li/Li_{10}SnP_2S_{12}/$ Li symmetric cells at relatively high nominal current densities of $\geq 1\,mA\,cm^{-2}$. Taking advantage of the high spatial resolution and fast scan times that are possible with a monochromatic synchrotron beam, we simultaneously resolved void formation, interphase evolution and electrode volume changes at the $Li/Li_{10}SnP_2S_{12}$ interface during cycling. Despite the substantial phase transformations

[1]School of Materials Science and Engineering, Georgia Institute of Technology, Atlanta, GA, USA. [2]George W. Woodruff School of Mechanical Engineering, Georgia Institute of Technology, Atlanta, GA, USA. [3]School of Mechanical Engineering, Purdue University, West Lafayette, IN, USA. [4]School of Energy and Chemical Engineering, Ulsan National Institute of Science and Technology, Ulsan, Republic of Korea. [5]Advanced Photon Source, Argonne National Laboratory, Lemont, IL, USA. ✉e-mail: mattmcdowell@gatech.edu

and volume changes that occur at the interfaces due to interphase formation, our quantitative analysis showed that cell failure was ultimately driven by interfacial void formation and contact loss that caused current constriction, providing important insight into SSB degradation mechanisms.

Operando X-ray tomography

The SSE studied in this work was $Li_{10}SnP_2S_{12}$ (LSPS). The crystal structure of pristine LSPS was verified using X-ray diffraction (Supplementary Fig. 1)[41]. Its conductivity was measured to be $2.1\,mS\,cm^{-1}$ at $20\,°C$ (Supplementary Fig. 2), which allows for cycling at current densities comparable to the targeted level for commercial cells[20]. However, the Li/LSPS interface will decompose through (electro)chemical reactions[42,43]. Previous X-ray photoelectron spectroscopy and nuclear magnetic resonance studies on this interphase have shown that Li_2S, Li_3P and Li–Sn alloys are formed[43], in agreement with computational predictions[11]. This interphase exhibits mixed-conducting properties, and therefore the reaction with lithium is not self-passivating[11]. Although these interfacial reactions are undesirable, the high conductivity of LSPS provides a route to understanding the complex coupled dynamics that occur at Li/SSE interfaces when cycled at realistic current densities.

Operando X-ray computed microtomography experiments were conducted at beamline 2-BM at the Advanced Photon Source. A custom solid-state cell was designed to apply a stack pressure to a 2-mm-diameter Li/LSPS/Li stack while maintaining an airtight seal (Fig. 1a). This smaller cell diameter compared with conventional research-grade SSB cells[21,35] was critical to achieve sufficient X-ray transmission. Monochromatic X-rays with an energy of $28\,keV$ were used because of an absorption edge of LSPS at $29.2\,keV$ (Supplementary Fig. 3). The entire stack was positioned within the field of view with a voxel size of $1.7\,\mu m$ and a rotational tomographic scan time of $7\,min$. Full details are presented in the Methods section.

Operando electrochemical cycling of the symmetric Li/LSPS/Li cells was carried out with tomography scans interspersed at $15\,min$ time intervals during the application of current. Galvanostatic voltage curves of two different cells cycled at 4 and $1\,mA\,cm^{-2}$ are shown in Fig. 1b,c, respectively. These voltage curves are comparable to those measured in a larger SSB cell ex situ (Supplementary Fig. 4). In the first half-cycle of both experiments, over $4\,mAh\,cm^{-2}$ of charge was transferred, corresponding to a theoretical lithium thickness of over $20\,\mu m$. Under these conditions, the cells experienced a rapid increase in voltage towards the end of each half-cycle (except for the first half-cycle in Fig. 1c). Small voltage shifts of $\sim10\,mV$ were observed during X-ray exposure, which we attribute to X-ray interactions generating photoelectrons that contribute to the measured voltage.

Figure 1d–i shows cross-sectional images of the Li/LSPS/Li symmetric cells before and after plating and stripping at $4\,mA\,cm^{-2}$ (Fig. 1d,g) and $1\,mA\,cm^{-2}$ (Fig. 1e,h). The contrast in the images is generated on the basis of differences in the X-ray attenuation coefficients of the materials[26]. Contrast between the LSPS with a higher average atomic number Z (brighter regions) and the lower Z lithium metal electrodes (darker regions) is clearly seen. A small fraction ($\sim7\%$) of the reconstructed images contain ring artefacts (Supplementary Fig. 5c,d). However, the majority of these artefacts are located in the bulk of LSPS away from the interfacial regions of interest for our analysis. Other artefacts or impurities that manifest as localized bright spots in the lithium electrodes are also present (Supplementary Fig. 5e–h). Fortunately, these artefacts only occupy a small percentage ($\sim0.1\%$) of the electrode volume, and in most cases they are away from the interface and do not affect our analysis.

For both experiments, the images after cycling (Fig. 1g,h) reveal changes in the lithium morphology as a consequence of plating and stripping, as well as the formation of an intermediate-contrast inter-

phase during plating. The lighter contrast of the interphase is due to reaction and incorporation of additional Li into the LSPS[23], lowering the average atomic number. Magnified views of the same Li/LSPS interface before and after one cycle at $1\,mA\,cm^{-2}$ are shown in Fig. 1f,i. Before cycling (Fig. 1f), the lithium and LSPS are in physical contact at the interface, despite the roughness present. After cycling, there are distinct regions with a darker contrast than that of lithium metal at the Li/SSE interface (Fig. 1i); the location of these regions suggests that they represent interfacial voids.

Line scans of the normalized image intensity at different interfaces demonstrate that the darker-contrast regions are formed during stripping and exhibit a lower intensity than lithium metal (Supplementary Fig. 6). Their intensity is similar to pores within the LSPS bulk (Supplementary Fig. 6), further indicating that they are voids. The formation of voids at the interface is consistent with electrochemical experiments in SSBs at high current densities[24,25]. Our operando X-ray tomography experiments were therefore able to successfully resolve interfacial voids. We partially attribute this result to the use of a monochromatic source, which improves sensitivity to X-ray absorption variations and removes beam-hardening effects.

Interphase formation

Reconstructed images reveal that a large amount of interphase is formed at the cathodic interface (Supplementary Fig. 7a,b). To determine the relative fractions of current contributing to interphase growth versus plating, we quantified the volumes of the interphase and the lithium electrodes in a subvolume (see Methods). The subvolume renderings in Fig. 2a show the interface as it is reduced at $1\,mA\,cm^{-2}$, demonstrating that the interphase grows continuously. Figure 2b plots the volume changes of the interphase and the cathodic lithium electrode (visualized in Fig. 2a), as well as the volume of the anodic lithium electrode at the opposite interface. As expected, the anodic lithium volume decreases as lithium is removed and transported to the cathodic interface. However, the lithium volume at the cathodic interface does not increase with time, which should occur if lithium metal is being deposited. Simultaneously, the interphase volume at this interface increases substantially. This analysis shows that the current at the cathodic interface results in electrochemical interphase formation rather than lithium deposition, and that the lithium metal electrode at this interface is actually slightly consumed due to the chemical reaction that also contributes to interphase formation. Cycling at a higher current density results in similar electrochemical processes (Supplementary Fig. 7c). These findings are important because although interphase formation is well documented[10,12,13,42], the extent to which this process affects electrochemistry in various materials is not well understood. Because no metal deposition occurs, we use the terminology 'reduction' instead of 'plating' herein. A consequence of the substantial interphase growth is that no lithium filaments were observed and there were no short circuits in our experiments, whereas ex situ X-ray imaging has previously shown filaments in argyrodite SSEs after cycling[34]. The lack of short circuiting is similar to previous results with other SSEs that form a mixed-conducting interphase[13,23,44].

Using the measured reduction of lithium metal volume during oxidation, we analysed the fraction of the total current arising from lithium metal stripping. For the first and second half-cycles of the experiment at $1\,mA\,cm^{-2}$ (Fig. 1c), these current fractions are 0.72 and 0.51, respectively. Thus, a large portion of the current results from interphase oxidation instead of lithium metal stripping; indeed, reversible interphase redox activity has been shown in other SSEs[15,42,45]. Additional operando experiments at a higher nominal current density ($4\,mA\,cm^{-2}$, Supplementary Fig. 9) further showed that an increasing fraction of the current comes from oxidation of the interphase as the interphase thickness increases (Fig. 2c).
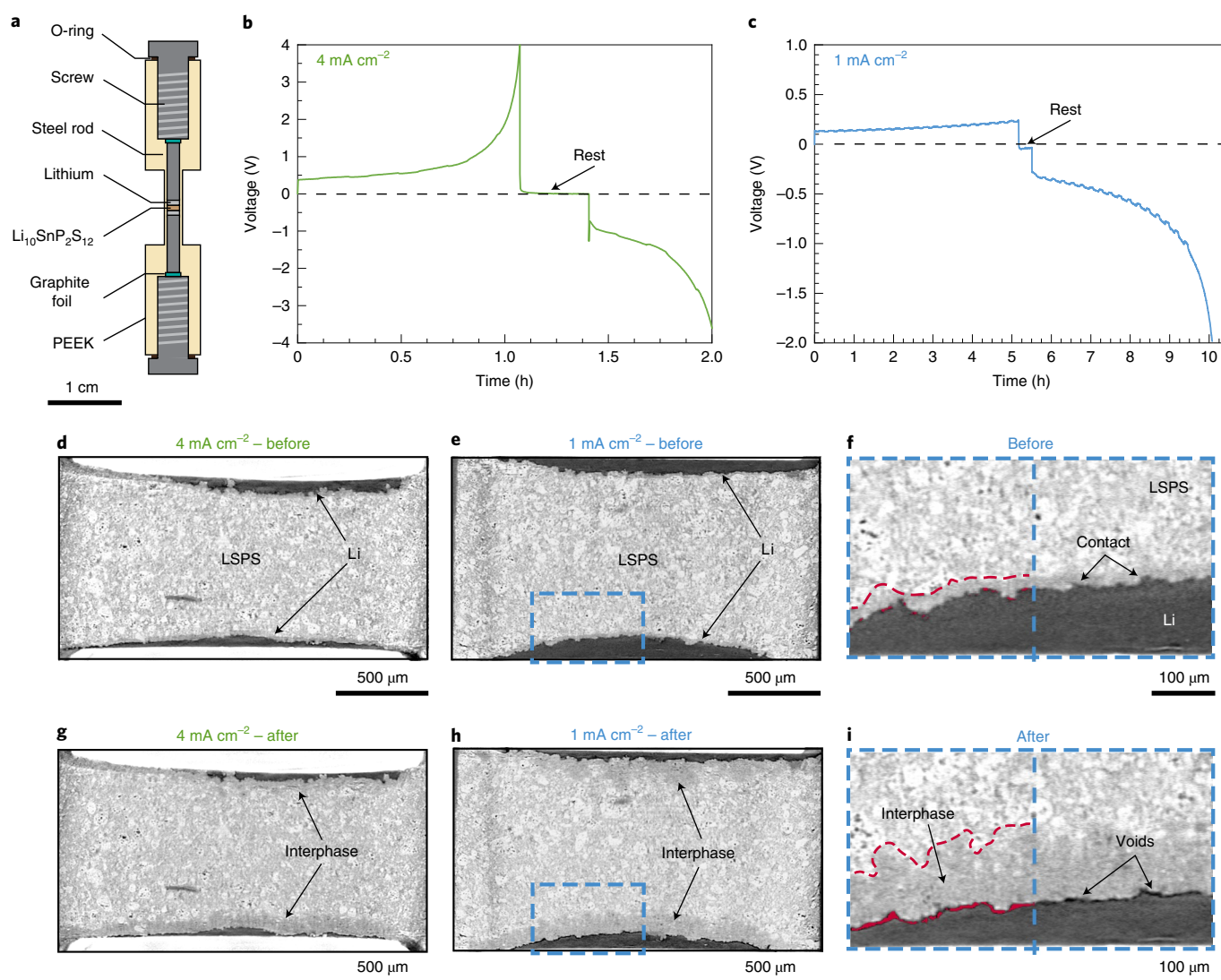
Fig. 1 | Operando X-ray imaging of cells at two current densities. a, Schematic of the custom X-ray tomography cell used to cycle Li/LSPS/Li cells during operando experiments. PEEK, polyether ether ketone. **b,c**, Galvanostatic voltage curves measured during operando experiments at 4 mA cm⁻² (**b**) and 1 mA cm⁻² (**c**). **d,e**, Reconstructed cross-sectional images before cycling at 4 mA cm⁻² (**d**) and 1 mA cm⁻² (**e**); these images are extracted from the 3D tomographic datasets. The regions with dark contrast are the lithium electrodes, whereas the grey phase is the LSPS electrolyte. The steel current collectors are also visible with white contrast at the top and bottom of **d**. **f**, Magnified cross-section of the Li/LSPS interface before cycling at 1 mA cm⁻², taken from the blue-boxed region in **e**. In the left half of the image, voids are overlaid with red for easier visualization, and the red dashed line above demarcates the interphase boundary; the right half of the image is unmarked. **g,h**, Cross-sectional images from the same locations as those shown in **d,e** after the electrochemical cycling procedure shown in **b,c**. The formation of an intermediate-contrast interphase can be seen at the interfaces, along with morphological changes in the lithium electrodes. **i**, Magnified cross-section of the same interface as shown in **f** after one full cycle at 1 mA cm⁻². The volume of voids at the interface has increased substantially (overlaid with red on the left half of the image), along with growth of the interphase (demarcated by the red dashed line in the left half of the image).

Void formation and contact loss at the Li/LSPS interface

The observed formation of voids at the Li/LSPS interfaces is expected to play an important role in cell stability. An automated segmentation procedure was developed to distinguish interfacial voids from other phases, such as lithium metal, LSPS and internal porosity (see Methods). This analysis allowed us to identify voids across the entire Li/LSPS interface and quantitatively link their evolution to electrochemistry. Figure 3a displays a segmented 3D subvolume at the Li/LSPS interface during stripping that shows the interphase and voids that form between LSPS and the lithium electrode. These renderings were taken from the second half-cycle of the cell tested at 1 mA cm⁻² (Fig. 1c). From these renderings, it is clear that the volume of the voids grows substantially after 3.0 mAh cm⁻² have been stripped.

Three different types of interfacial void evolution were observed. Each subfigure in Fig. 3b–d shows the two-dimensional reconstructed image of the same location at the Li/SSE interface before and after an electrochemical process, with the segmented interfacial voids coloured red for visibility; Supplementary Fig. 10 contains the images without the red overlays. The most common process is the formation of voids during stripping (Fig. 3b). Voids form during stripping when Li⁺ ions are removed faster than the lithium metal can be replenished, either through self-diffusion or mechanical deformation. Void formation during stripping is consistent with recent studies that have demonstrated polarization at the stripping electrode[24,25,46]. We also analysed the possible influence of interface morphology on void formation (Supplementary Fig. 11
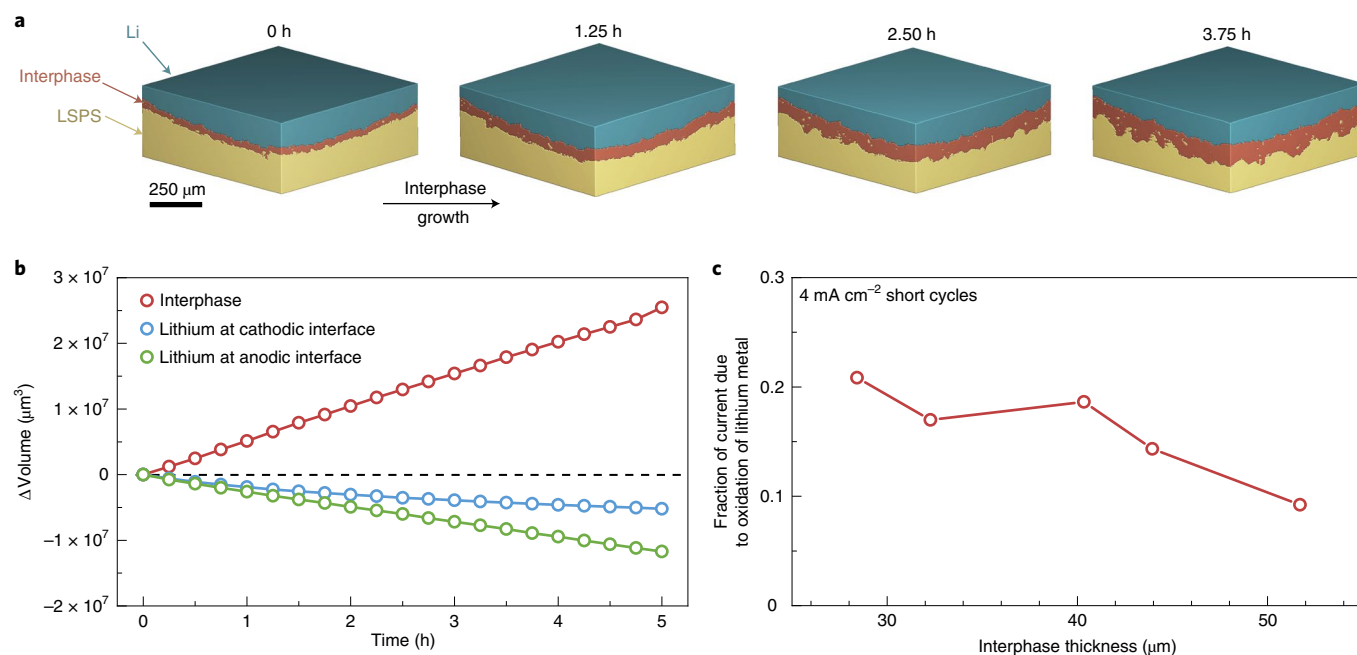
Fig. 2 | Analysis of interphase growth and electrochemical behaviour. a, Three-dimensional renderings of a $680 \times 680 \times 340\,\mu m$ subvolume at the Li/LSPS interface over time during reduction at $1\,mA\,cm^{-2}$. Segmentation routines (see Methods) were used to visualize the lithium metal (blue), interphase (red) and LSPS (yellow). The size and location of these subvolumes are shown in Supplementary Fig. 8a. **b**, Plot showing the change in volume of the interphase at this interface, as well as both lithium electrodes, during the first half-cycle at $1\,mA\,cm^{-2}$. The interphase and cathodic lithium volumes were taken from the subvolume shown in **a**, whereas the anodic lithium volume was taken from a subvolume with the same size at the opposite interface (not shown). **c**, Fraction of total current due to oxidation of lithium metal, plotted as a function of the interphase thickness. These data were taken from an operando experiment with 30 min cycles at a current density of $4\,mA\,cm^{-2}$ (Supplementary Fig. 9); these conditions were used to steadily grow the interphase thickness. Note that a lower fraction of the current comes from oxidation of lithium metal at $4\,mA\,cm^{-2}$ compared with lower current densities.

and Supplementary Methods). Notably, our analysis shows that the tendency to form voids during stripping is independent of local interfacial roughness. The second phenomenon we observed is the closing of voids during reduction (Fig. 3c). Despite there being no measurable lithium deposition to fill the voids, we suspect that local compression due to interphase growth can close them, but this process was not observed in every experiment. The third phenomenon observed is the formation of voids at the cathodic interface (Fig. 3d). This behaviour is counterintuitive, as mass is being added at this interface. However, the lithium electrode is being consumed due to a chemical side reaction (see Fig. 2b), which probably results in such void formation.

The image contrast between voids and lithium enables the real-time determination of how the contact area influences the electrochemistry. Figure 4a shows how the total Li/LSPS contact areas across the entire top and bottom interfaces change over time for the cell cycled at $1\,mA\,cm^{-2}$. Stripping occurs at the top interface for the first ~5.5 h, after which stripping begins at the bottom interface. The electrochemical signature in the first half-cycle shows only a minor increase in overpotential, which is reflected in the relatively invariant contact areas at both interfaces. After cycling for ~9 h, the cell begins to rapidly polarize to −4 V, during which the interfacial contact area at the bottom interface decreases by 52%. We note that in this two-electrode experiment, the voltage includes contributions from impedance at both interfaces.

The observed correlation between the interfacial contact and the increase in cell voltage suggests that the loss of contact at the anodic interface drives cell failure. To investigate these effects, we implemented an electrochemical model with our cell geometry that incorporates Butler–Volmer kinetics at the Li/SSE interface, as well as transport in the SSE and the growing interphase (see Methods). Figure 4b shows the results for the situation in which the voltage of

the first half-cycle was matched to the experiment through choice of interphase conductivity and interfacial exchange current density. These conditions were then used to predict the voltage of the second half-cycle on the basis of the experimentally measured contact area variation of the bottom interface without taking into account the contact geometry. The predicted magnitude of the cell voltage under these conditions is much lower than the measured value. Reducing the contact area in simulations of the second half-cycle increases the overpotential (Fig. 4b), but matching to the experiment requires the imposition of an extremely low contact area (Supplementary Fig. 12).

We visualized the spatiotemporal evolution of contact at each interface by creating contact area maps from the segmented datasets (Fig. 4c,d). These contact area maps show the contact area across the entire interface throughout cycling, with coloured pixels (green for the top interface and yellow for the bottom interface) representing contact between lithium and the interphase/LSPS, and black pixels in the maps indicating no contact (that is, either an interfacial void or no lithium is present). At time = 0 h, there are already numerous regions without interfacial contact that are probably the result of insufficient stack pressure[35]. This means that the effective current density is actually 4–5 times higher than the nominal value. The contact area maps for the top interface (Fig. 4c) show that there is only minor contact loss throughout the entire experiment. However, Supplementary Fig. 13 shows that the physical locations of contact at this interface shift during stripping, which emphasizes the dynamic nature of these interfaces. The contact area maps of the bottom interface (Fig. 4d) show a more substantial change in contact distribution. A contact loss of −8.9% occurs over the first 4 h during reduction. A dramatic contact loss of −47.1% at the bottom interface occurs over the last 0.75 h during stripping, which corresponds to the period of rapid cell polarization. The contact loss at
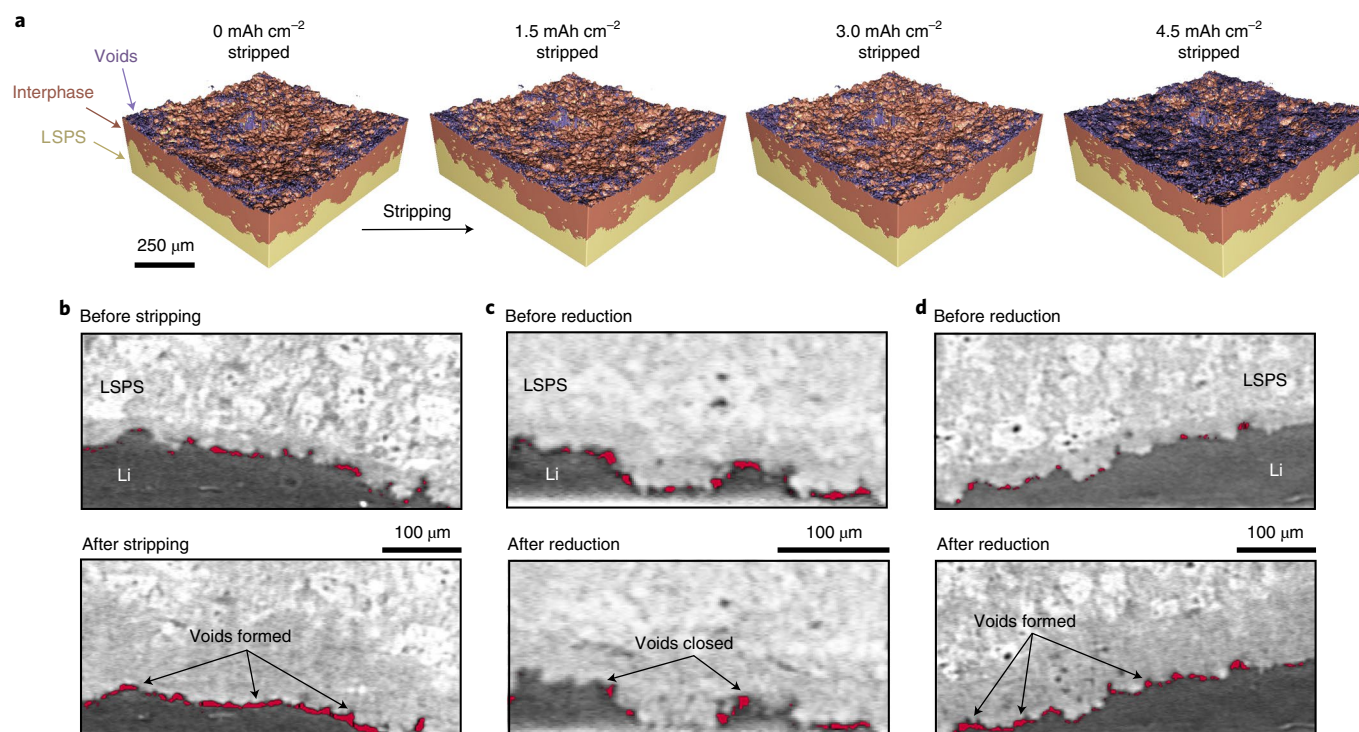
Fig. 3 | Evolution of voids at the Li/LSPS interface. a, Three-dimensional segmented renderings of the Li/LSPS interface at different times during stripping at 1 mA cm⁻², with the total areal capacity stripped shown above each image. The renderings show the voids (purple), the interphase (red) and LSPS (yellow). The renderings represent the same region as shown in Fig. 2a. **b**, Two-dimensional cross-sectional images of the Li/LSPS interface before (top) and after (bottom) stripping at 1 mA cm⁻². Pixels identified as voids during the segmentation process are overlaid with red, showing that void growth occurs during stripping. **c**, Cross-sectional images of the Li/LSPS interface before (top) and after (bottom) reduction at 4 mA cm⁻² show that voids can be closed during reduction. **d**, Cross-sectional images before (top) and after (bottom) reduction at 1 mA cm⁻² show that voids can also be formed during reduction.

the bottom interface is greater in the final hour of cycling than during first nine hours.

The contact analysis suggests that the discrepancy between the predicted and experimental voltage curves is probably due to current constriction from spatial reconfiguration and the loss of interfacial contact. Current constriction can occur when interfacial contact locations are relatively small compared to the nominal interfacial area, which causes distortion of current lines and the creation of constriction resistance[46–48]. The phenomenon of current constriction is well established in other types of solid–solid interfaces[47], but it has only recently been proposed as a key factor in lithium-based SSBs in a study that found that the constriction in bulk ion transport near the Li/Li$_{6.25}$Al$_{0.25}$La$_3$Zr$_2$O$_{12}$ interface is responsible for high interfacial impedance[46]. As shown in Fig. 4d, the large, continuously contacting regions present initially at the bottom interface are broken up into small isolated contacting spots by the end of the experiment. Before cycling, 71% of the total contact area at this interface is contained within two large regions with areas of 0.42 and 0.19 mm², whereas the remaining 29% comes from separated contact regions with individual areas of less than 0.02 mm² (see Supplementary Fig. 14). After stripping, 100% of the contact area is supplied by separated contact regions with areas less than 0.02 mm². The increase of small, isolated contact spots will greatly enhance current constriction effects, which probably drives the substantial cell polarization. Other factors could also include redox and possible mass transport limitations of the interphase.

As shown here, operando X-ray computed microtomography enables quantification of the spatial distribution of physical contact at Li/SSE interfaces. However, these experiments probably provide an overestimate of the contact area, since the spatial resolution was not sufficient to resolve all microscopic voids or atomic-scale vacancies. Importantly, our results allow for the monitoring of micron-scale contact changes across the entire field of view of the interface, thus capturing how the interfacial contact changes impact the electrochemistry. We therefore conclude that the loss of contact at the stripping interface is the underlying phenomenon that leads to cell failure in this system.

The evolution of contact is expected to affect behaviour at all solid-state electrochemical interfaces. Indeed, similar polarization behaviour has been observed during lithium plating/stripping experiments with Li$_{6.25}$Al$_{0.25}$La$_3$Zr$_2$O$_{12}$ (LLZO)[46], which is the most stable SSE against lithium metal, as well as sodium/Na-β″-alumina interfaces[39], suggesting that our results are relevant to solid-state interfaces beyond lithium. To explore polarization behaviour in different SSEs, we conducted ex situ electrochemical experiments with the argyrodite-type SSE material Li$_6$PS$_5$Cl (LPSC) in symmetric cells (see Supplementary Methods). Unlike LSPS, LPSC forms a kinetically stabilized interphase versus lithium[35], which minimizes interphase growth but also enables lithium filaments to penetrate the material. At a current density of 0.8 mA cm⁻², the cell short-circuited due to filament growth before any substantial polarization could occur (Supplementary Fig. 15a). The lower current density of 0.4 mA cm⁻² avoided filament growth but led to severe polarization beyond 2.0 V after a few hours (Supplementary Fig. 15b), much like the Li/LSPS/Li cells shown in Figs. 1 and 4 and resembling other LPSC results[24]. The electrochemical similarities between LSPS, LLZO and LPSC indicate that the operando experiments in this work capture interfacial contact phenomena that are relevant to a wide range of SSE materials.
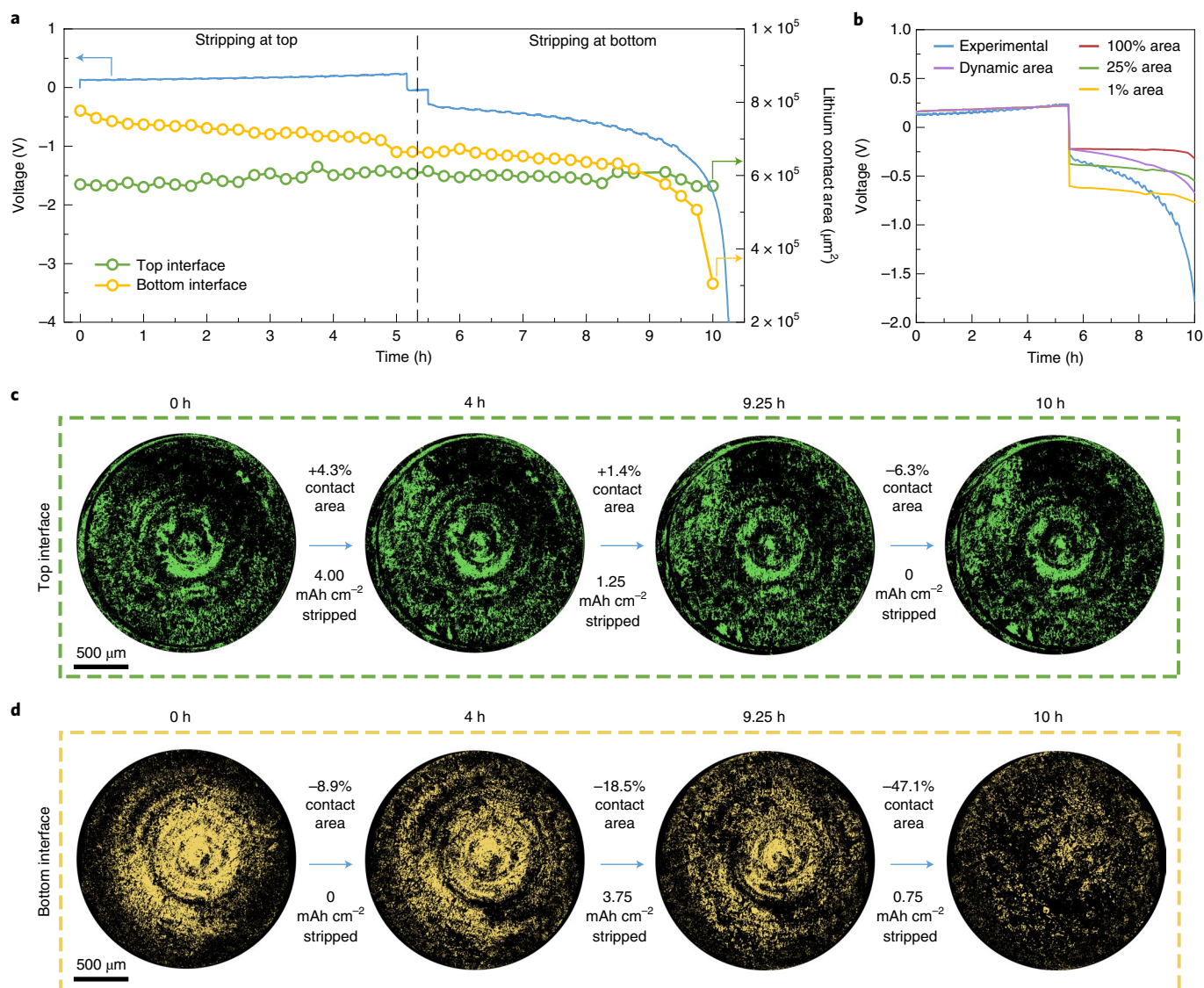
Fig. 4 | Relating interfacial contact area to cell electrochemistry. a, Plot of the voltage curve measured during cycling at 1 mA cm^{-2} (blue line) and the corresponding total lithium contact area of the top (green) and bottom (yellow) Li/LSPS interfaces in this cell. **b**, Comparison between the experimental voltage curve (blue) and theoretically predicted voltage curves using 100% (red) of the experimental contact area in the second half-cycle, 25% (green), 1% (yellow) and the dynamically varied contact area (purple). **c**, Contact area maps of the entire top Li/LSPS interface throughout the experiment. The percentage change in contact area and lithium capacity removed between maps are indicated. **d**, Contact area maps of the entire bottom Li/LSPS interface throughout the experiment. In **c** and **d**, coloured pixels indicate the presence of interfacial contact at that location, while black pixels indicate a lack of contact (that is, a void or no lithium is present at that location). The initial ring-like spatial arrangement of contacting (coloured) pixels in the leftmost panel in **c**,**d** arises because of slight ring-shaped non-uniformities on the surface of the steel rods that apply the stack pressure.

Volumetric changes and partial molar volume mismatch

Our dataset also enables the analysis of volume changes and displacements throughout the cell. Figure 5a shows a portion of a lithium electrode that decreases in volume during stripping at 1 mA cm^{-2}. The Li/SSE interface moves upwards by ~17 μm (indicated by the red lines) due to the lithium electrode receding and the simultaneous expansion of the interphase at the opposite interface. Through this process, however, the current collector also moves downwards by ~20 μm (blue lines). Additional analysis showed that the LSPS pellet undergoes non-uniform displacements during cycling, as shown by the vector field map with fivefold scaling in Fig. 5b. The maximum displacement measured in the SSE is ~20 μm, which is consistent with the upward movement of the Li/LSPS interface in the previous half-cycle (Fig. 5a). The LSPS material thus moves non-uniformly towards the anodic interface, with greater displace-

ments near the centre of the pellet compared with the edges of the pellet that probably result in shear strain and non-uniform stresses.

Analysis of a subvolume showed that the volume of the cell stack (that is, all materials between the current collectors) decreases during cycling (Fig. 5c), as also suggested by the observed displacement of the LSPS pellet coupled with the displacement of the current collector. Since the overall electrochemical process involves stripping lithium at one interface to form an interphase at the other, this net volume loss can be explained if the partial molar volume of lithium in the interphase is less than in lithium metal. Indeed, the partial molar volume of lithium in most battery cathodes and binary compounds is less than that in lithium metal, and these compounds are expected to be present within the interphase[22,49]. As a result of this partial molar volume mismatch, the LSPS pellet and current collectors are displaced during cycling and there is a net decrease in
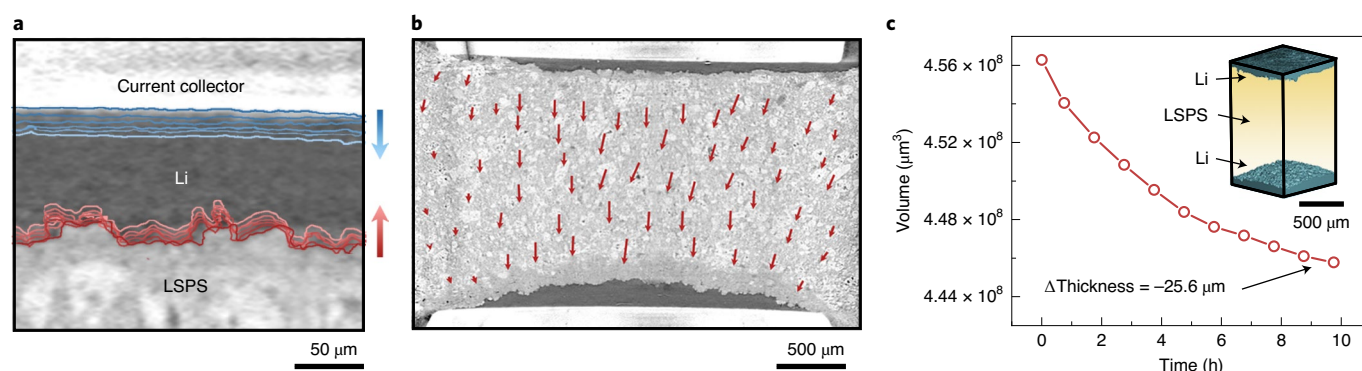
Fig. 5 | Displacements and volume changes within a cell. a, The position of the Li/LSPS interface and the current collector tracked during stripping of the lithium. The arrows indicate the direction of motion of each interface: darker lines represent positions at earlier times during the stripping, with the transition to lighter lines as stripping proceeds. **b**, Vector map showing physical displacements of the point at the base of each vector as lithium is stripped from the bottom interface at a current density of 1 mA cm^{-2}. The magnitude of each vector is scaled by a factor of five for visual clarity. **c**, Measured volume of a subvolume consisting of the entire Li/LSPS/Li stack during cycling at 1 mA cm^{-2}. The analysed subvolume was $680 \times 680 \times 1,360$ μm and is visualized in the inset, with lithium metal in blue and LSPS in yellow. The size and location of this subvolume relative to the entire volume is shown in Supplementary Fig. 8b. The total change in thickness of this cell stack at the end of cycling was -25.6 μm.

cell volume. The different magnitudes of the displacements within the LSPS occur because the lithium electrodes at the edges of the cell are thinner, resulting in less interphase growth at these locations. Electrochemical cycling of an ex situ Li/LSPS/Li cell outfitted with a force sensor (Supplementary Fig. 16) shows decreasing stack pressure during cycling, which we suspect is due to volume loss within the cell. Manually increasing the stack pressure of the operando tomography cell between experiments was found to increase the contact area and decrease the cell voltage (Supplementary Fig. 17). Thus, we conclude that the partial molar volume mismatch and volume loss in our cells leads to a decreased stack pressure, which could exacerbate the overpotential increases.

Our observation of cell-volume shrinkage is different from that expected for Li/SSE/Li symmetric cells that undergo only lithium plating/stripping, as there would be no partial molar volume mismatch between the electrodes. Importantly, however, our results are relevant for designing full cells that contain a lithium metal anode and a cathode material since lithium has a lower partial molar volume in most cathode materials than in lithium metal[22], which will result in an overall reduction in cell volume during discharge. Our results highlight the chemo-mechanical challenges in creating full cells with controlled stack pressure throughout cycling[21,22,50], and they also indicate that commonly studied Li/SSE/Li symmetric cells are not entirely representative of the chemo-mechanical conditions present in full cells.

This investigation has revealed the dynamic evolution of lithium interfaces in SSBs and has directly shown that the loss and reconfiguration of interfacial contact is the critical factor that causes cell failure. The chemo-mechanical phenomena we have observed herein are expected to play important roles during the operation of SSBs on the basis of a wide variety of SSE chemistries beyond LSPS, as supported by our experiments with LPSC. Contact evolution/current constriction and volumetric changes are inherent challenges in SSBs, and nearly all SSEs decompose to some extent to form an interphase. Our results, along with continued use of operando X-ray tomography and other such techniques, will help to guide the development of SSBs with high energy densities and long lifetimes. In particular, the dynamics of lithium filament growth and the effects of incorporating different composite cathodes are key scientific aspects that require greater understanding for the successful integration of lithium metal within SSBs. We have shown that it is possible to conduct operando imaging to quantify contact loss at Li/SSE interfaces, which could help to elucidate how lithium filaments nucleate and grow during charge. Considering the wider application of this characterization method, different SSEs will exhibit different extents of X-ray attenuation, which will affect the contrast at interfaces; furthermore, the observation of dynamic processes would benefit from faster tomographic scan times (<7 min). It is also important to study how volume change mismatches between electrodes in full-cell architectures can alter mechanical stress throughout the cell[21,22]. Material displacements, localized stress variations and the loss of stack pressure caused by introducing a cathode could have an impact on contact at the Li/SSE interface, and thus the electrochemical performance of full SSBs.

Online content

Any methods, additional references, Nature Research reporting summaries, source data, extended data, supplementary information, acknowledgements, peer review information; details of author contributions and competing interests; and statements of data and code availability are available at https://doi.org/10.1038/s41563-020-00903-2.

References

1. Manthiram, A., Yu, X. & Wang, S. Lithium battery chemistries enabled by solid-state electrolytes. *Nat. Rev. Mater.* **2**, 16103 (2017).
2. Famprikis, T., Canepa, P., Dawson, J. A., Islam, M. S. & Masquelier, C. Fundamentals of inorganic solid-state electrolytes for batteries. *Nat. Mater.* **18**, 1278–1291 (2019).
3. Tan, D. H. S., Banerjee, A., Chen, Z. & Meng, Y. S. From nanoscale interface characterization to sustainable energy storage using all-solid-state batteries. *Nat. Nanotechnol.* **15**, 170–180 (2020).
4. Janek, J. & Zeier, W. G. A solid future for battery development. *Nat. Energy* **1**, 16141 (2016).
5. Zhang, Z. et al. New horizons for inorganic solid state ion conductors. *Energy Environ. Sci.* **11**, 1945–1976 (2018).
6. Lewis, J. A., Tippens, J., Cortes, F. J. Q. & McDowell, M. T. Chemo-mechanical challenges in solid-state batteries. *Trends Chem.* **1**, 845–857 (2019).
7. Xiao, Y. et al. Understanding interface stability in solid-state batteries. *Nat. Rev. Mater.* **5**, 105–126 (2020).
8. Hatzell, K. B. et al. Challenges in lithium metal anodes for solid-state batteries. *ACS Energy Lett.* **5**, 922–934 (2020).
9. Richards, W. D., Miara, L. J., Wang, Y., Kim, J. C. & Ceder, G. Interface stability in solid-state batteries. *Chem. Mater.* **28**, 266–273 (2016).
10. Zhu, Y., He, X. & Mo, Y. Origin of outstanding stability in the lithium solid electrolyte materials: insights from thermodynamic analyses based on

first-principles calculations. *ACS Appl. Mater. Interfaces* **7**, 23685–23693 (2015).

11. Ong, S. P. et al. Phase stability, electrochemical stability and ionic conductivity of the $Li_{10\pm1}MP_2X_{12}$ (M = Ge, Si, Sn, Al or P, and X = O, S or Se) family of superionic conductors. *Energy Environ. Sci.* **6**, 148–156 (2013).

12. Wenzel, S. et al. Direct observation of the interfacial instability of the fast ionic conductor $Li_{10}GeP_2S_{12}$ at the lithium metal anode. *Chem. Mater.* **28**, 2400–2407 (2016).

13. Lewis, J. A. et al. Interphase morphology between a solid-state electrolyte and lithium controls cell failure. *ACS Energy Lett.* **4**, 591–599 (2019).

14. Wenzel, S. et al. Interphase formation and degradation of charge transfer kinetics between a lithium metal anode and highly crystalline $Li_7P_3S_{11}$ solid electrolyte. *Solid State Ion.* **286**, 24–33 (2016).

15. Schwietert, T. K. et al. Clarifying the relationship between redox activity and electrochemical stability in solid electrolytes. *Nat. Mater.* **19**, 428–435 (2020).

16. Cheng, E. J., Sharafi, A. & Sakamoto, J. Intergranular Li metal propagation through polycrystalline $Li_{6.25}Al_{0.25}La_3Zr_2O_{12}$ ceramic electrolyte. *Electrochim. Acta* **223**, 85–91 (2017).

17. Porz, L. et al. Mechanism of lithium metal penetration through inorganic solid electrolytes. *Adv. Energy Mater.* **7**, 1701003 (2017).

18. Han, F. et al. High electronic conductivity as the origin of lithium dendrite formation within solid electrolytes. *Nat. Energy* **4**, 187–196 (2019).

19. Kazyak, E. et al. Li penetration in ceramic solid electrolytes: operando microscopy analysis of morphology, propagation, and reversibility. *Matter* **2**, 1025–1048 (2020).

20. Randau, S. et al. Benchmarking the performance of all-solid-state lithium batteries. *Nat. Energy* **5**, 259–270 (2020).

21. Zhang, W. et al. (Electro)chemical expansion during cycling: monitoring the pressure changes in operating solid-state lithium batteries. *J. Mater. Chem. A* **5**, 9929–9936 (2017).

22. Koerver, R. et al. Chemo-mechanical expansion of lithium electrode materials – on the route to mechanically optimized all-solid-state batteries. *Energy Environ. Sci.* **11**, 2142–2158 (2018).

23. Tippens, J. et al. Visualizing chemomechanical degradation of a solid-state battery electrolyte. *ACS Energy Lett.* **4**, 1475–1483 (2019).

24. Kasemchainan, J. et al. Critical stripping current leads to dendrite formation on plating in lithium anode solid electrolyte cells. *Nat. Mater.* **18**, 1105–1111 (2019).

25. Wang, M. J., Choudhury, R. & Sakamoto, J. Characterizing the Li-solid-electrolyte interface dynamics as a function of stack pressure and current density. *Joule* **3**, 2165–2178 (2019).

26. Pietsch, P. & Wood, V. X-ray tomography for lithium ion battery research: a practical guide. *Annu. Rev. Mater. Res.* **47**, 451–479 (2017).

27. Lin, F. et al. Synchrotron X-ray analytical techniques for studying materials electrochemistry in rechargeable batteries. *Chem. Rev.* **117**, 13123–13186 (2017).

28. Shen, F., Dixit, M. B., Xiao, X. & Hatzell, K. B. Effect of pore connectivity on Li dendrite propagation within LLZO electrolytes observed with synchrotron X-ray tomography. *ACS Energy Lett.* **3**, 1056–1061 (2018).

29. Dixit, M. B. et al. Nanoscale mapping of extrinsic interfaces in hybrid solid electrolytes. *Joule* **4**, 207–221 (2020).

30. Wu, X. et al. Operando visualization of morphological dynamics in all-solid-state batteries. *Adv. Energy Mater.* **9**, 1901547 (2019).

31. Sun, F. et al. Visualizing the morphological and compositional evolution of the interface of InLi-anode|thio-LISION electrolyte in an all-solid-state Li–S cell by in operando synchrotron X-ray tomography and energy dispersive diffraction. *J. Mater. Chem. A* **6**, 22489–22496 (2018).

32. Kimura, Y. et al. Influence of active material loading on electrochemical reactions in composite solid-state battery electrodes revealed by operando 3D CT-XANES imaging. *ACS Appl. Energy Mater.* **3**, 7782–7793 (2020).

33. Dixit, M. B. et al. Synchrotron imaging of pore formation in Li metal solid-state batteries aided by machine learning. *ACS Appl. Energy Mater.* https://doi.org/10.1021/acsaem.0c02053 (2020).

34. Seitzman, N. et al. Toward all-solid-state lithium batteries: three-dimensional visualization of lithium migration in β-Li_3PS_4 ceramic electrolyte. *J. Electrochem. Soc.* **165**, A3732 (2018).

35. Doux, J. M. et al. Stack pressure considerations for room-temperature all-solid-state lithium metal batteries. *Adv. Energy Mater.* **10**, 1903253 (2020).

36. Harry, K. J., Hallinan, D. T., Parkinson, D. Y., MacDowell, A. A. & Balsara, N. P. Detection of subsurface structures underneath dendrites formed on cycled lithium metal electrodes. *Nat. Mater.* **13**, 69–73 (2014).

37. Madsen, K. et al. Direct observation of interfacial mechanical failure in thiophosphate solid electrolytes with operando X-ray tomography. *Adv. Mater. Interfaces* **7**, 2000751 (2020).

38. Dixit, M. et al. In situ investigation of chemomechanical effects in thiophosphate solid electrolytes. *Matter* https://doi.org/10.1016/j.matt.2020.09.018 (2020).

39. Jolly, D. S. et al. Sodium/Na β″ alumina interface: effect of pressure on voids. *ACS Appl. Mater. Interfaces* **12**, 678–685 (2019).

40. Neumann, A. et al. Analysis of interfacial effects in all-solid-state batteries with thiophosphate solid electrolytes. *ACS Appl. Mater. Interfaces* **12**, 9277–9291 (2020).

41. Bron, P. et al. $Li_{10}SnP_2S_{12}$: an affordable lithium superionic conductor. *J. Am. Chem. Soc.* **135**, 15694–15697 (2013).

42. Tarhouchi, I., Viallet, V., Vinatier, P. & Ménétrier, M. Electrochemical characterization of $Li_{10}SnP_2S_{12}$: an electrolyte or a negative electrode for solid state Li-ion batteries? *Solid State Ion.* **296**, 18–25 (2016).

43. Zheng, B. et al. Unraveling (electro)-chemical stability and interfacial reactions of $Li_{10}SnP_2S_{12}$ in all-solid-state Li batteries. *Nano Energy* **67**, 104252 (2020).

44. Cortes, F. J. Q., Lewis, J. A., Tippens, J., Marchese, T. S. & McDowell, M. T. How metallic protection layers extend the lifetime of NASICON-based solid-state lithium batteries. *J. Electrochem. Soc.* **167**, 050502 (2020).

45. Han, F., Gao, T., Zhu, Y., Gaskell, K. J. & Wang, C. A battery made from a single material. *Adv. Mater.* **27**, 3473–3483 (2015).

46. Krauskopf, T., Hartmann, H., Zeier, W. G. & Janek, J. Toward a fundamental understanding of the lithium metal anode in solid-state batteries – an electrochemo-mechanical study on the garnet-type solid electrolyte $Li_{6.25}Al_{0.25}La_3Zr_2O_{12}$. *ACS Appl. Mater. Interfaces* **11**, 14463–14477 (2019).

47. Greenwood, J. A. Constriction resistance and the real area of contact. *Brit. J. Appl. Phys.* **17**, 1621–1632 (1966).

48. Krauskopf, T., Richter, F. H., Zeier, W. G. & Janek, J. Physicochemical concepts of the lithium metal anode in solid-state batteries. *Chem. Rev.* **120**, 7745–7794 (2020).

49. Ahmad, Z. & Viswanathan, V. Stability of electrodeposition at solid–solid interfaces and implications for metal anodes. *Phys. Rev. Lett.* **119**, 056003 (2017).

50. Mistry, A. & Mukherjee, P. P. Molar volume mismatch: a malefactor for irregular metallic electrodeposition with solid electrolytes. *J. Electrochem. Soc.* **167**, 082510 (2020).

Methods

Cell assembly. LSPS was purchased from NEI Corporation. A custom X-ray tomography cell was built for the operando synchrotron X-ray tomography experiments. The cell body was constructed from polyether ether ketone to minimize X-ray attenuation and to prevent short circuiting between the electrodes. The inner diameter was 2 mm to minimize the sample size, ensuring sufficient transmission to image the cell. The assembly of symmetric Li/LSPS/Li cells was carried out inside an argon-filled glovebox. A portion of LSPS (7 mg) was loaded into the cell and pressed at 225 MPa to form a pellet approximately 1 mm thick. Lithium metal foils were punched out and attached to steel rods, which were then inserted into each side of the cell. To establish the pressure necessary to cycle these cells at high current densities, screws were used to compress the rods against the faces of the pellet. O-rings attached to the screw heads were simultaneously compressed to form a seal when the screw was inserted. The torque applied to the screws was 0.25 N m (estimated to be greater than 10 MPa) for each experiment unless otherwise specified. Graphite foils were placed between the steel rods and screws to prevent the rods from rotating and damaging the Li/SSE interface. All operando electrochemical measurements were performed using a Bio-Logic SP-150 potentiostat.

Synchrotron X-ray computed microtomography experiments. Operando X-ray computed microtomography experiments were conducted at the Advanced Photon Source's 2-BM beamline. Monochromatic X-rays with an energy of 28 keV were chosen to maximize transmission in our samples on the basis of attenuation length calculations (Supplementary Fig. 3). Fifteen hundred projections were taken with an exposure time of 210 ms while rotating the sample through 180°. An Oryx 5.0 MP Mono 10GigE detector and a ×2 magnification lens were used just for the optics in this setup. The sample-to-detector distance for all experiments was 100 mm. We were able to achieve a voxel size of 1.7 μm while fitting the entire sample within the field of view of ~4.2 × 1.4 mm². The time required to complete a scan under these conditions was approximately 7 min. The raw data were reconstructed with TomoPy using the Gridrec method[51].

Segmentation analysis. *Lithium segmentation.* The reconstructed images were segmented using MATLAB to identify the lithium volumes across the entire 3D dataset. A dynamic cropping procedure was applied to select the appropriate regions of interest. Schematic representations of the MATLAB procedures used to segment the regions of interest for different phases are shown in Supplementary Figs. 18–20. To identify lithium metal (Supplementary Fig. 18), the cropped reconstructed images were analysed by traversing columns of pixels from the top to the bottom of the image. The sharp difference in intensity between the steel rod and the lithium electrode was used to define the upper boundary of the lithium. Traversing downward from the upper boundary, the algorithm continued to recognize pixels as lithium as long as their intensity was below the specified intensity cutoff typical for lithium (Supplementary Fig. 18). The identification of lithium in a single pixel column stopped when the average intensity of the next five pixels was above a threshold value for LSPS (see Supplementary Fig. 18). The pixel intensity values for lithium were typically 2–3 times lower and had a lower standard deviation than the pixel intensity values of either LSPS or interphase. This process was repeated for every column until the entire 2D image was segmented; the algorithm was then used to segment each 2D image within the 3D tomographic dataset to identify the entire volume of the lithium electrodes. Analysis using subvolumes was performed by selecting specific regions within these segmented electrodes. Three-dimensional renderings of the subvolumes were created using the Dragonfly software platform.

Void segmentation. Void segmentation was performed using a separate algorithm in MATLAB. The segmentation process is schematically illustrated in Supplementary Fig. 19. The algorithm traversed pixel columns in 2D image slices from the bulk of the LSPS pellet toward the lithium electrode while identifying pixels with intensities below an intensity cutoff typical for voids. Once such a pixel was found, the algorithm continued identifying the neighbouring pixels in the column with intensities below the void cutoff to determine the height of the void. After continued traversal, the algorithm would reach the lithium metal; once the average intensity of five adjacent pixels was representative of lithium metal (that is, typical of the lithium intensity and below the LSPS threshold), all of the identified void pixels were segmented as an interfacial void. If the average intensity of the pixels above the void was higher than the LSPS threshold (that is, representing LSPS instead of lithium), then the identified void was recognized as a pore in LSPS and was ignored. The algorithm would then continue until an interfacial void was identified or the end of the column was reached. This process was repeated for every column in each 2D image, and subsequently for every image along the interface in the 3D tomographic dataset. Three-dimensional renderings of the subvolumes were created using the Dragonfly software platform.

Contact area mapping. The contact area maps were created through further analysis in MATLAB (Supplementary Fig. 20). After identifying lithium in every pixel column of a 2D reconstructed image (Supplementary Fig. 18), the contact area algorithm evaluated the five pixels in each column at the edge of

the lithium electrode in search of values below the lithium intensity and typical of void intensity. If any of these five pixels had an intensity below the void cutoff intensity (that is, a void is present at the interface), that pixel column was marked as exhibiting no contact at the interface. Otherwise, the pixel column was marked as contacting at the interface. The image slice was then regenerated containing only columns that were marked as having contact. This procedure was performed on every 2D slice of the entire 3D Li/LSPS interface. The modified slices were then projected onto a 2D plane perpendicular to the image slices, yielding a 2D map of the contact area for the entire interface, and these are the contact area maps shown in Fig. 4c,d. In these images, coloured pixels represent regions where lithium contacts LSPS, whereas black pixels represent regions with either interfacial voids or no lithium present. The contact area for an interface was calculated by measuring the number of coloured pixels and using the voxel dimensions to convert this value to a physical area.

Interphase segmentation. The interphase volumes were segmented using the WEKA trainable segmentation package built into FIJI/ImageJ. This analysis was conducted using 680 × 680 × 340 μm subvolumes to reduce the computational requirements and to improve accuracy. Classifiers for LSPS, lithium and the interphase were created and then manually identified over many cross-sections. These inputs were then used to train a model that could identify the classified phases over the entire subvolume. The resulting RGB images were then binarized in MATLAB to isolate the interphase class and analysed to measure the interphase volume and thickness. Similar procedures were used to segment the LSPS from the porosity within the pellet; ten different 340 × 340 × 340 μm subvolumes were segmented to yield an average LSPS pellet density of 96.8 ± 0.9%.

Electrochemical model. An electrochemical model for a symmetric cell configuration was developed that takes into account the contact areas at the top and bottom interfaces, growth of the interphase and the electrolyte conductivity. The kinetic overpotentials at the top and bottom interfaces were calculated using the Butler–Volmer expression.

$$i_{BV,j} = \frac{I}{A_j} = i_0 \left(\exp\left(\frac{\alpha_a F}{RT} \eta \right) - \exp\left(-\frac{\alpha_c F}{RT} \eta \right) \right), \quad j = \text{top, bottom}$$
$$\eta = \phi_s - \phi_e - U_{Li}, \quad U_{Li} = 0.0 \text{ V}$$

Here, $i_{BV,j}$ refers to the reaction current density at the jth interface (j = top or bottom), which was evaluated using the ratio of applied current magnitudes, I, with respect to the experimentally extracted contact areas A_j (distinct for the top and bottom interfaces). The variables i_0, α_a, α_c and η refer to the exchange current density, the anodic and cathodic charge-transfer coefficients and the kinetic overpotential, respectively. The kinetic overpotential is a function of the solid-phase and electrolyte-phase potentials (ϕ_s and ϕ_e respectively), as well as the equilibrium potential U_{Li} of the lithium plating/stripping reaction. The potential drops across the electrolyte and interphase were calculated as follows:

$$\Delta \phi_j = \frac{i_{app} l_j}{\kappa_j}, \quad j = \text{electrolyte, interphase}$$

where i_{app}, κ_j and l_j correspond to the applied current density, ionic conductivity (electrolyte or interphase), and thickness (electrolyte or interphase), respectively. Here, the applied current density is assumed to be the average of the current densities at the top and bottom interfaces. It is to be noted that the interphase thickness evolves over time and this input is derived from the experimental data. The cell voltage was computed by summing the contributions from the ohmic and kinetic potential drops, which have been described above. Owing to the high electronic conductivity of lithium metal, the ohmic drop across the metal electrode was neglected in the above analysis.

Data availability

Source data are provided with this paper. All other data that support results in this Article are available from the corresponding author upon reasonable request.

Code availability

MATLAB codes developed for segmentation and analysis of tomographic data in this paper are available from the corresponding author upon reasonable request.

References

51. Gürsoy, D., de Carlo, F., Xiao, X. & Jacobsen, C. TomoPy: a framework for the analysis of synchrotron tomographic data. *J. Synch. Radiat.* **21**, 1188–1193 (2014).

Acknowledgements

Author contributions

M.T.M., J.A.L. and F.J.Q.C. conceived the study. J.A.L., F.J.Q.C., Y.L. and T.S.M. conducted the operando X-ray tomography experiments. J.A.L., J.C.M. and J.T. designed and tested the cell housings, with C.S. guiding the preliminary imaging experiments. J.A.L. and D.P. conducted the preliminary ex situ cycling experiments. S.Y.H. and C.L. developed pressure measurements for the cell housings. P.P.S. created the three-dimensional renderings. F.D.C. and P.S. assisted with the use of beamline 2-BM and reconstruction processing. A.V., B.S.V. and P.P.M. developed the electrochemical model. J.A.L. and F.J.Q.C. segmented and analysed the data, and also wrote the manuscript with M.T.M. All authors commented on the manuscript.

Competing interests

The authors declare no competing interests.

Additional information

Supplementary information is available for this paper at https://doi.org/10.1038/s41563-020-00903-2.

Correspondence and requests for materials should be addressed to M.T.M.

Peer review information *Nature Materials* thanks Ying Meng and the other, anonymous, reviewer(s) for their contribution to the peer review of this work.

Reprints and permissions information is available at www.nature.com/reprints.